Borehole-to-surface wave propagation: modeling with finite elements

Pierre Samec and Clement Kostov

ABSTRACT

Finite element computations (two space dimensions, cartesian geometry) are used to illustrate wave propagation phenomena for models including a fluid-filled borehole and a free-surface. We show that at low frequencies, such that the "diameter" of the borehole is small compared to the wavelength, the borehole significantly influences the far field by conversion of tube waves to Rayleigh and body waves. Our results are relevant to seismic experiments where the source is in a borehole and the receivers are either near the surface or in another borehole.

INTRODUCTION

The material properties in a volume several tens or hundreds of meters around a borehole are of interest for drilling operations, forecasting, and monitoring of fluid flow.

A standard VSP experiment probes such a volume; however new experiments, such as cross-hole tomography or transposed VSP, could eventually provide better data. A related experiment is the transposed VSP that uses drill-bit noise as source signal.

Wave propagation phenomena near the borehole are complex. A variety of elastic wave modes are created at interfaces having strong contrasts in material properties. This occurs between air and rock along the free surface, or between fluid and rock in the borehole. The waves of interest for imaging of the formation are the body P and S waves from the downhole source. Other wavetypes, including surface and body waves, are generated at discontinuities along the interface.

Depending on the position of the geophones, the "noise" wavemodes may have dominant amplitudes with respect to the "signal", and thus create a difficult situation for the processing of data from such experiments. To understand the wave

propagation phenomena involved in the experiments mentioned above, we apply the finite element method to the modeling of elastic waves propagating in a two-dimensional, cartesian geometry. We present several examples of conversions between wavemodes that may occur at a free surface or at an interface.

WHY FINITE ELEMENTS ?

The borehole and the rock formation are two media with very different material properties and scales. A borehole has a diameter of about 0.3 m. To represent adequately the fields within the borehole the grid spacing should be about 0.05 m. In the rock, the wavelength is greater than 3 m for frequencies of the wavelet less than 1000 Hz. Clearly, the density of grid points in the rock could be reduced by at least a factor of 10.

The finite element method is particularly well-suited to the modeling of waves propagating on an irregular grid. (Strang, 1986, Sword et al., 1986) We therefore choose a finite element numerical scheme for the problem at hand.

LAGRANGIAN METHOD AND FINITE ELEMENTS

Notations and Conventions

Some notations and conventions, used in the following presentation of the finite element method applied to the propagation of elastic waves, are summarized in the present section.

Symbol	Description
C_{ijkl}	Elastic tensor, function of space coordinates ($C_{ijkl}(x,y,z)$)
ρ	Density
u	Displacement field
u^i_j	j^{th} component of the displacement field at node i
$u_{i,j}$	Partial derivative of the i^{th} coordinate with respect to the j^{th} coordinate
σ_{ij}	Stress tensor
e_{ij}	Strain tensor defined as $e_{ij} = \frac{1}{2}(u_{i,j} + u_{j,i})$
δ_{ij}	Kroenecker delta symbol
$\dot{u}$	Partial derivative in time of the displacements field
$\frac{\partial}{\partial t}$	partial derivative operator in time
k	Wave number
$\omega = 2\pi f$	Frequency: f in Hz, and ω in radians/sec.
FT	Fourier transform in space and time.

Lagrangians for elastic waves and fluids

The Lagrangian for elastic waves can be shown to be

$$\mathbf{L} = \mathbf{KE} - \mathbf{PE} = \frac{1}{2}\rho\dot{u}^2 - c_{ijkl}e_{ij}e_{kl}, \tag{1}$$

where **L** is the lagrangian, **KE** is the kinetic energy of the system, and **PE** is the potential energy. (Morse and Feshbach, 1953)

The equations of motion, or Lagrange's equations, are then :

$$\frac{d}{dt}\left(\frac{\partial \mathbf{L}}{\partial \dot{u}_j}\right) = \frac{\partial \mathbf{L}}{\partial u_j}. \tag{2}$$

The Lagrangian for a fluid is

$$\mathbf{L} = -\frac{1}{2}\rho\left((\nabla(\phi))^2 - \frac{1}{c^2}\left(\frac{\partial\phi}{\partial t}\right)^2\right),$$

where the field velocity is $\nabla\phi$, and the pressure in the fluid is $\frac{\rho}{c^2} \times \frac{\partial\phi}{\partial t}$. (Morse and Feshbach, 1953):

Below, computations will be carried explicitly for the solid only (Equations (1) and (2)); similar equations can be derived for the fluid.

Finite element approximation of the Lagrange's equations

Discretizating the Lagrange's equations on a finite element grid, requires a means by which all fields on the grid can be interpolated independently from the element shape. For example,

$$u_i = u_i^j X^j. \tag{2}$$

where X^j is a function only of the relative position within the element. So as to compute X^j three sets of coordinates are introduced following the denominations given by Zienkiewicz (1973) :

1) the physical coordinates x,y,z,
2) the nodal coordinates ϵ, η, τ,
3) the generalized coordinates a_1, a_2, a_3.

Figure 1 illustrates the first two sets of coordinates. We will assume that they are linearly related as follows:

$$x(\epsilon) = < \bar{N}_1, \bar{N}_2, ...\bar{N}_n > \begin{bmatrix} x^1 \\ x^2 \\ \\ \\ x^n \end{bmatrix}, \tag{3}$$

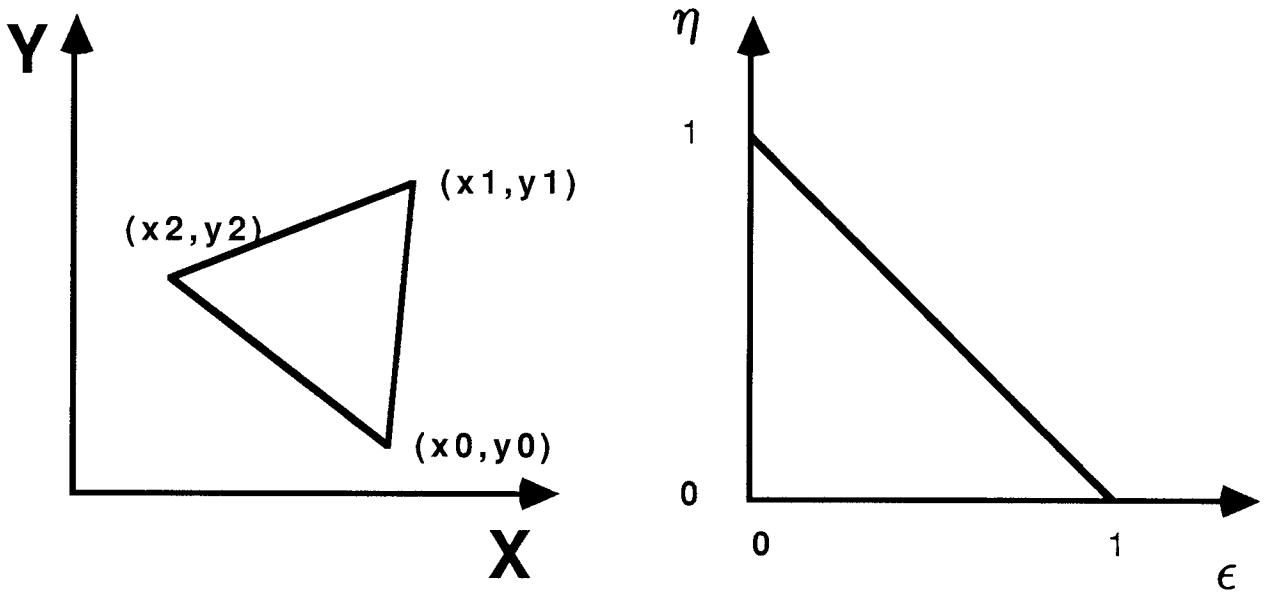

FIG. 1. Transform from physical to nodal coordinates.

and

$$u_i(\epsilon) = < N_1, N_2, ...N_n > \begin{bmatrix} u_i^1 \\ u_i^2 \\ \\ \\ u_i^n \end{bmatrix}. \tag{4}$$

Given a set of interpolation polynomials, $P_i(\epsilon)$, the generalized coordinates a_1, a_2, a_3 can now be defined as follows:

$$u(\epsilon) = P_j(\epsilon)a_j.$$

This last set of coordinates must verify

$$u^i = P_j(\epsilon^i)a_j, \tag{5}$$

where ϵ_j is the nodal coordinate of node i (Figure 1). We then have from Equations (3), (4), and (5)

$$u(\epsilon) = P_j(\epsilon)[P_j(\epsilon^i)]^{-1}u^i = < N_i > u_i. \tag{6}$$

This relation also applies for the coordinates within one element, so long as the number of independent interpolation functions is equal to the number of nodes defining one element. In that case $N_j = \bar{N}_j$. Elements defined by this property are called isoparametric elements. An important property of such elements is that the interpolated fields are continuous not only within elements, but also across boundaries of elements.

The interpolation polynomials for the triangular isoparametric element (used in the numerical examples presented below) are:

$$P_1(\epsilon) = 1, \quad P_2(\epsilon) = \epsilon, \quad P_3(\epsilon) = \eta.$$

The interpolated field within an element is then:

$$u_j(\epsilon,\eta) = (1 - \epsilon - \eta)u_j^1 + \eta u_j^2 + \epsilon u_j^3, \tag{7}$$

where

$$N_1(\epsilon) = 1 - \epsilon - \eta \quad N_2(\epsilon) = \eta \quad N_3(\epsilon) = \epsilon.$$

Other operations such as derivation and integration also need to be performed in nodal coordinates to discretize Equation (2). The derivative operators in physical and nodal coordinates are linearly related by the following expression,

$$\begin{bmatrix} \frac{\partial}{\partial x} \\ \frac{\partial}{\partial y} \end{bmatrix} = \left[\begin{pmatrix} \frac{\partial \epsilon}{\partial x} & \frac{\partial \eta}{\partial x} \\ \frac{\partial \epsilon}{\partial x} & \frac{\partial \eta}{\partial y} \end{pmatrix} \right] \begin{bmatrix} \frac{\partial}{\partial \epsilon} \\ \frac{\partial}{\partial \eta} \end{bmatrix} = \mathbf{J}^{-1} \begin{bmatrix} \frac{\partial}{\partial \epsilon} \\ \frac{\partial}{\partial \eta} \end{bmatrix},$$

where $\mathbf{J}$ denotes the Jacobian of the transformation from nodal to physical coordinates.

Using the finite element approximation (Equations (4),(5),(6)) the Jacobian $\mathbf{J}$ can be expressed in terms of the values at the nodes of the grid as:

$$\mathbf{J} = \begin{bmatrix} \frac{\partial}{\partial \epsilon} \\ \frac{\partial}{\partial \eta} \end{bmatrix} < x, y > = \begin{bmatrix} N_{1,\epsilon} \\ N_{2,\eta} \end{bmatrix} < x^n, y^n > .$$

To derive the discrete strain tensor, let $\mathbf{J}^{-1} = (a_{ij})$, and apply the previous relations to express the derivative operators in nodal coordinates:

$$e_{ij} = \frac{1}{2}\left(a_{j1}(-u_i^1 + u_i^3) + a_{j2}(-u_i^1 + u_i^2) + a_{i1}(-u_j^1 + u_j^3) + a_{i2}(-u_j^1 + u_j^2)\right). \tag{8}$$

Integration can be performed similarly using again the Jacobian of the transformation from physical to nodal coordinates.

Derivation of the discretized wave equation for elastic anisotropic media

To obtain a set of discrete linear equations, Equation (1) will now be integrated using finite element techniques. The domain of integration chosen here will be the cluster of elements connected to one node. (Sword et al., 1986)

Let ψ denote the domain defined by one element, and S, the cluster. From Equation (7) we can then write :

$$\frac{d}{dt}\frac{\partial}{\partial \dot{u}_i^1}\left[\int_\psi \mathbf{KE}\right] = \rho\frac{A}{12}(2\ddot{u}_i^1 + \ddot{u}_i^2 + \ddot{u}_i^3),$$

$$\frac{d}{dt}\frac{\partial}{\partial \dot{u}_i^1}\left[\int_S \mathbf{KE}\right] = \rho\frac{A}{12}(2n_c\ddot{u}_i^1 + \sum_{n=1}^{n_c}\ddot{u}_i^n), \tag{9}$$

A being the area of one subdomain, assumed constant here for each element, and n_c the number of elements connected to one node. When a cluster contains domains with different areas, Equation (9) can be rewritten in a more general form as:

$$\frac{d}{dt}\frac{\partial}{\partial \dot{u}_i^1}\left[\int_S \mathbf{KE}\right] = = 2m(1)\ddot{u}_i^1 + \sum_{n=1}^{n_c} m(k+1)\ddot{u}_i^n.$$

Similarly, using Equations (1) and (8) we have:

$$\frac{\partial e_{ij}}{\partial u_m} = -\frac{\delta_{im}}{2}(a_{j1} + a_{j2}) - \frac{\delta_{jm}}{2}(a_{i1} + a_{i2}),$$

$$\frac{\partial}{\partial u_m}\left[\int_{S_d} \mathbf{PE}\right] = 2\sum_{n=1}^{n_c}\left[c_{ijkl}\frac{\partial e_{ij}}{\partial u_m}e_{kl}\right]. \tag{10}$$

Finally, assembling Equations (9) and (10), we can write two equations for each node:

$$m(1)\ddot{u}_1^1 + \sum_{n=1}^{n_c} m(n+1)\ddot{u}_1^n = C_1u_1^1 + C_2u_2^1 + \sum_{n=1}^{n_c}\alpha_1(n)u_1^n + \sum_{n=1}^{n_c}\alpha_2(n)u_2^n, \tag{11}$$

and

$$m(1)\ddot{u}_2^1 + \sum_{n=1}^{n_c} m(n+1)\ddot{u}_2^n = C_3u_1^1 + C_4u_2^1 + \sum_{n=1}^{n_c}\alpha_3(n)u_1^n + \sum_{n=1}^{n_c}\alpha_4(n)u_2^n. \tag{12}$$

The coefficients in the above system verify the following properties:

$$m(1) = \sum_{n=1}^{n_c} m(n+1) \qquad \text{with} \qquad \mathrm{m(n)} > 0, \tag{13}$$

and

$$C_i = \sum_{n=1}^{n_c} -\alpha_i(n) \quad \text{with} \qquad \mathrm{C_i} < 0.$$

Note that all $m(n)$, $n \neq 1$, are equal when all elements in a cluster have the same area.

Assembling Equation (11) for all the nodes of the discretized structure, we have:

$$\mathbf{M}(\ddot{u}) = \mathbf{A}(u) + f, \tag{14}$$

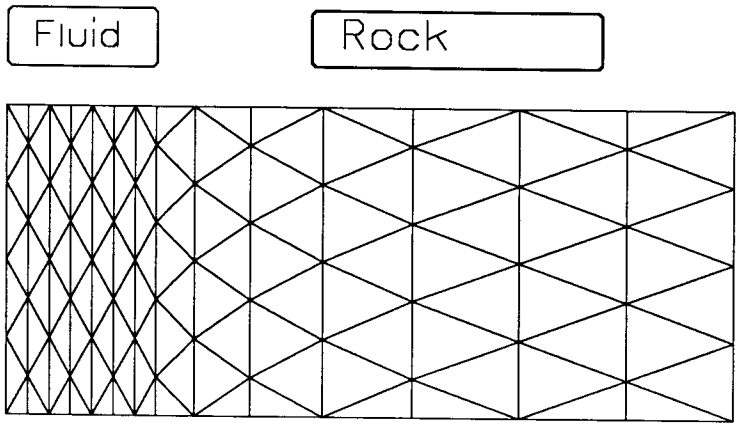

FIG. 2. Example of a finite element grid. The stretching factor is 5 along the horizontal axis.

f being the vector representing the discretized external forces acting on the grid.

Using an explicit finite element algorithm in time we have:

$$u(t+\Delta t) \;=\; \Delta t^2 \mathbf{M}^{-1}\left[\mathbf{A}(u) \;+\; f\right] \;+\; 2u(t) \;-\; u(t-\Delta t). \tag{15}$$

Before going further, a brief description of the properties of matrices **M** and **A** must be made. It can be shown from Equation (13) that **M** is symmetric positive definite, and **A** is symmetric negative definite. Matrices **A** and **M** are large, (10000×10000), but sparse (6 elements per row for **M** and 14 for **A** .) We also recognize that the diagonal terms in **M** are approximately ten times larger than the off-diagonal terms. Taking advantage of this matrix structure, the following method has been used to invert **M**:

$$\mathbf{M} \;=\; \mathbf{M}_d \;+\; \mathbf{M}_n, \tag{16}$$

where $\mathbf{M}_d$ is the diagonal part of **M**, and $\mathbf{M}_n$ the non diagonal part, and

$$\mathbf{M}^{-1} \approx \left[\mathbf{I} \;-\; \mathbf{M}_d^{-1}\mathbf{M}_n \;+\; (\mathbf{M}_d^{-1}\mathbf{M}_n)^2\right]\mathbf{M}_d^{-1}.$$

Numerical dispersion and grid anisotropy

The numerical dispersion introduced by the discretization is analyzed by applying Equations (11) and (12) to monochromatic plane waves. The Fourier transform

of the time-derivative operator in Equation (11) can be written as follows:

$$\mathbf{FT}\left[\frac{u_1^n(t+\Delta t) - 2u_1^n(t) + u_1^n(t-\Delta t)}{\Delta t^2}\right] =$$

$$= \mathbf{FT}\left(u_1^1(t)\right) e^{ik.(x_n - x_1)} \frac{2cos(\omega\Delta t) - 1}{\Delta t^2} e^{i\omega t} \approx$$

$$\approx -\omega^2 \mathbf{FT}\left(u_1^1(t)\right) e^{ik.(x_n - x_1)} e^{i\omega t}, \quad \text{for} \quad \omega\Delta t \ll 1.$$

The Fourier transform of Equations (11) and (12) can be written in matrix form as:

$$\lambda \begin{bmatrix} \mathbf{FT}(u_1) \\ \mathbf{FT}(u_2) \end{bmatrix} = \begin{pmatrix} a_1 & a_3 \\ a_2 & a_4 \end{pmatrix} \begin{bmatrix} \mathbf{FT}(u_1) \\ \mathbf{FT}(u_2) \end{bmatrix} \tag{17}$$

with

$$\lambda = -\omega^2 \left[m(1) + \sum_{n=1}^{n_c} m(n+1) e^{ik.(x_n - x_1)}\right],$$

and

$$a_j = C_j + \sum_{n=1}^{n_c} \alpha_j(n) e^{ik.(x_n - x_1)}.$$

From equation (17) we see that λ must be an eigenvalue of (a_{ij}) . It can be deduced from the matrix properties of $\mathbf{M}$ and $\mathbf{A}$ that (a_{ij}) is symmetric positive definite, and therefore λ must be positive and non zero. Let $-k^2c_1^2$ and $-k^2c_2^2$ be the eigenvalues of (a_{ij}). We then have for the real part of equation (17):

$$\lambda = -\omega^2 \left(m(1) + \sum_{n=1}^{n_c} m(n+1) e^{ik.(x_n - x_1)}\right) = -k^2c_i^2 \quad i = 1, 2.$$

Further for $k.(x_n - x_1) \ll 1$, i.e. for wavelengths much greater than the characteristic size of the element,

$$\lambda = -\omega^2 \left(2m(1) + \sum_{n=1}^{n_c} m(n+1)\phi^2(n)\right) = -k^2c_i^2, \quad i = 1, 2,$$

with $\phi(n) = k.(x_n - x_1)$.

Using the same order of approximation as for the inversion of matrix $\mathbf{M}$, we obtain the phase velocity of the medium :

$$v_{\phi_i} = \frac{c_i}{\sqrt{2m(1)}} \left(1 + \sum_{n=1}^{n_c} \frac{m(n+1)}{2m(1)} \phi^2(n)\right)^{-\frac{1}{2}} \approx$$

$$\frac{c_i}{\sqrt{2m(1)}} \left[1 - \frac{1}{2} \sum_{n=1}^{n_c} \frac{m(n+1)}{2m(1)} \phi^2(n) + \frac{3}{8} \left(\sum_{n=1}^{n_c} \frac{m(n+1)}{2m(1)} \phi^2(n)\right)^2 \ldots\right], \text{ with i } = 1, 2.$$

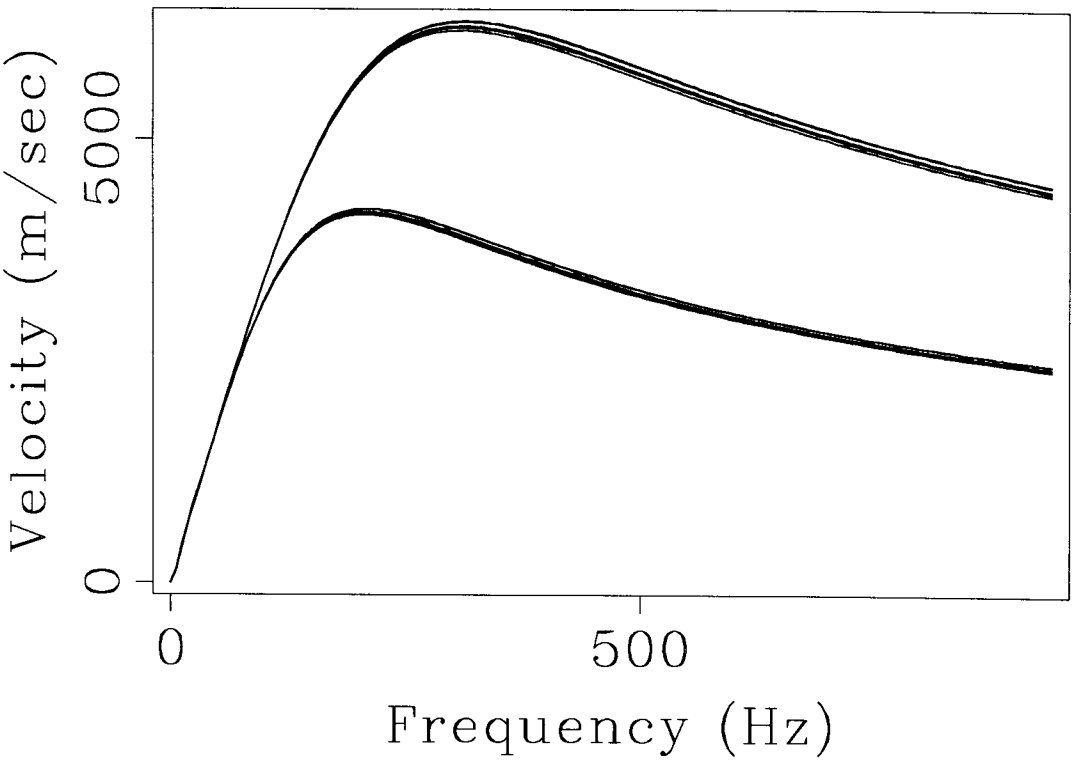

FIG. 3. Numerical dispersion and anisotropy for compressional and shear body waves. Each curve shows the group velocity as a function of frequency for a particular direction of propagation.

The group velocity can be deduced from:

$$v_{g_i} = \frac{\partial \omega}{\partial k} = k\frac{\partial v_{\phi_i}}{\partial k} + \frac{\omega}{k} \quad \text{with i} = 1,2,$$

where v_ϕ is the phase velocity, and v_g the group velocity. We found that the optimum accuracy is obtained for the third order of the expansion. This is the order that has been chosen for the explicit finite element formulation shown above. Figure 3 shows that for frequencies ranging from 0 to 1000 Hz, the simulated medium displays a large amount of dispersion. The dispersion is especially large around zero frequency, and creates the so-called "standing modes." However, the energy spectrum of the source wavelet is such that the amount of dispersion is minimized for the main part of the source signal.

Boundary conditions

Four types of boundary conditions are used for the models presented in the following sections. The first boundary is that which exists between fluid and rock. This boundary is modeled by coupling two independent structures – one for the fluid, and one for the liquid, (Zienkiewicz, 1967). In this way, nodes at the boundaries of each structure have the same spatial location, and the coupling is described by two equations stating the continuity of the normal displacements and the normal stresses (Figure 4).

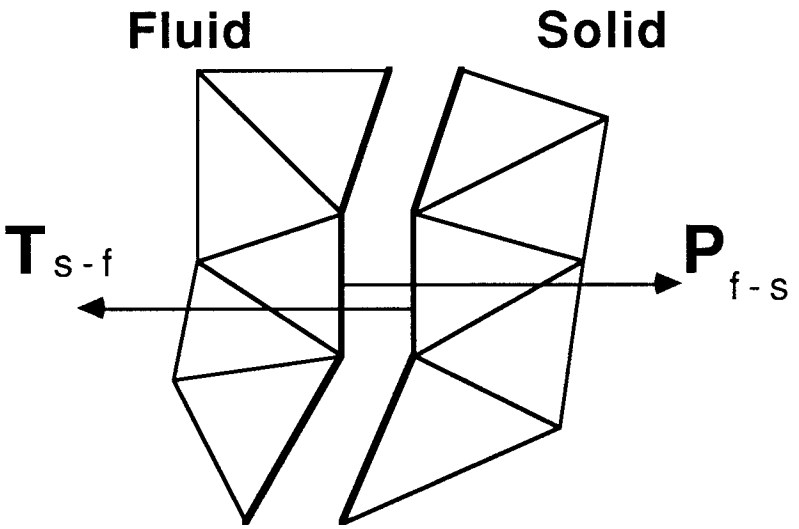

FIG. 4. Boundary conditions at the fluid-solid interface. P_{f-s} is the pressure, T_{s-f} is the traction.

The second boundary is the horizontal axis at the bottom of the structure. This axis is assumed to be an axis of symmetry for the whole system; therefore, zero vertical displacements are imposed on that axis.

The third type of boundary condition is applied to absorbing boundaries on the sides of the model. In order to avoid reflections on these boundaries, the displacement field is attenuated at each time step by a space dependent factor of the form $e^{-\left(\frac{|x-x_n|^2}{\delta^2}\right)}$, where $|x - x_n|$ is the horizontal distance between the node indexed by n and the edge of the grid. We obtained good energy absorption at the boundary with maximum gain factors of the order of .98 applied to the last twenty columns of elements. (A column is parallel to the borehole.)

The fourth and last type of boundary condition is used to achieve propagation only on one side of the borehole (Figures 11 and 12). Such an "opaque" boundary is obtained by imposing an infinite impedance contrast between the fluid and the rock.

NUMERICAL EXAMPLES

Vertical point source in an elastic layered medium

To start the wave propagation simulations with a familiar example, we computed the displacements of the wavefield radiated by a vertical point force (Aki and

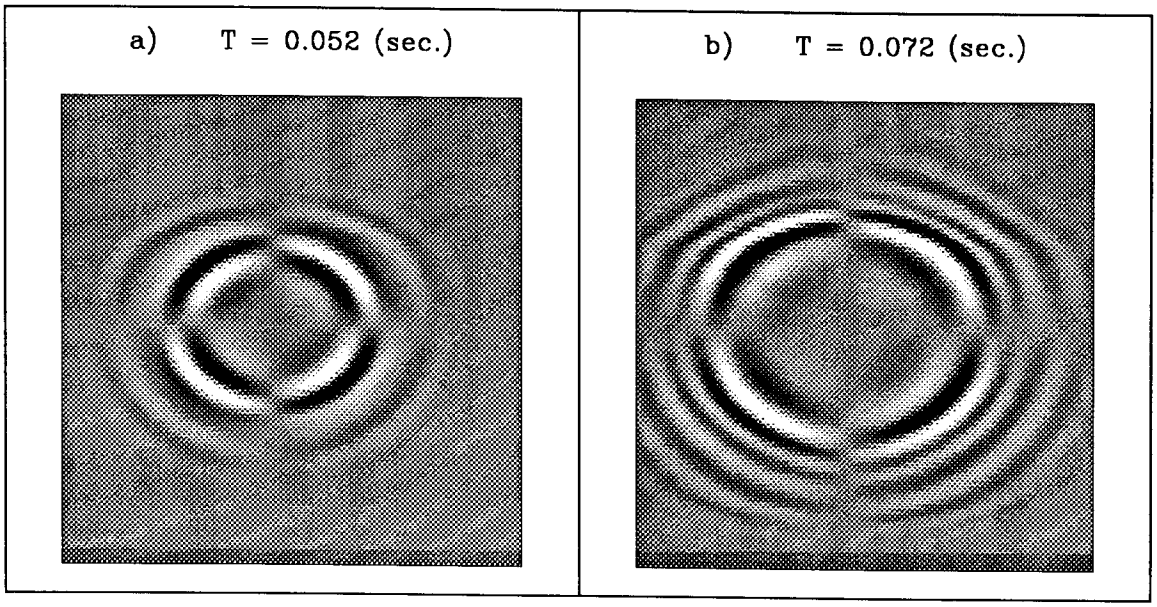

FIG. 5. Horizontal displacements of the wavefield generated by a vertical point force in a heterogeneous isotropic medium.

Richards, 1980, p.75). The dimensions of the model are 54 × 54 meters. The model contains three horizontal layers. The top and bottom layers have a compressional velocity of $v_p = 2.85$ km/sec and a shear velocity of $v_s = 1.92$ km/sec. The middle layer has a compressional velocity of $v_p = 4.3$ km/sec and a shear velocity of $v_s = 2.72$ km/sec.

The center frequency of the wavelet is about 350 Hz; its half-width is about 50 Hz. For 3000 time steps and a grid composed of 11,000 elements, the approximate CPU time on the Convex C1 was 11 minutes.

Figure 5 shows two snapshots of the horizontal displacements of the wavefield radiated by a vertical point force at the center of the finite element grid. The main features for this experiment are well reproduced (1) far-field radiation pattern with a 180° phase change between adjacent quadrants, (2) reflections at the interface between the fast and low medium, and (3) energy distribution between compressional and shear modes in a ratio of about $\frac{v_S^2}{v_P^2} \approx 0.5$. There is some dispersion as indicated by the ringing of the wavelet. The value of the field in the center of the grid is small, although not exactly zero, because of the standing modes previously mentioned.

Source in a fluid-filled borehole surrounded by a homogeneous medium

The following examples illustrate the coupling between borehole and rock. The downhole source is composed of vertical point forces applied at all grid points along the bottom of the borehole (seven point sources). The rock surrounding the borehole

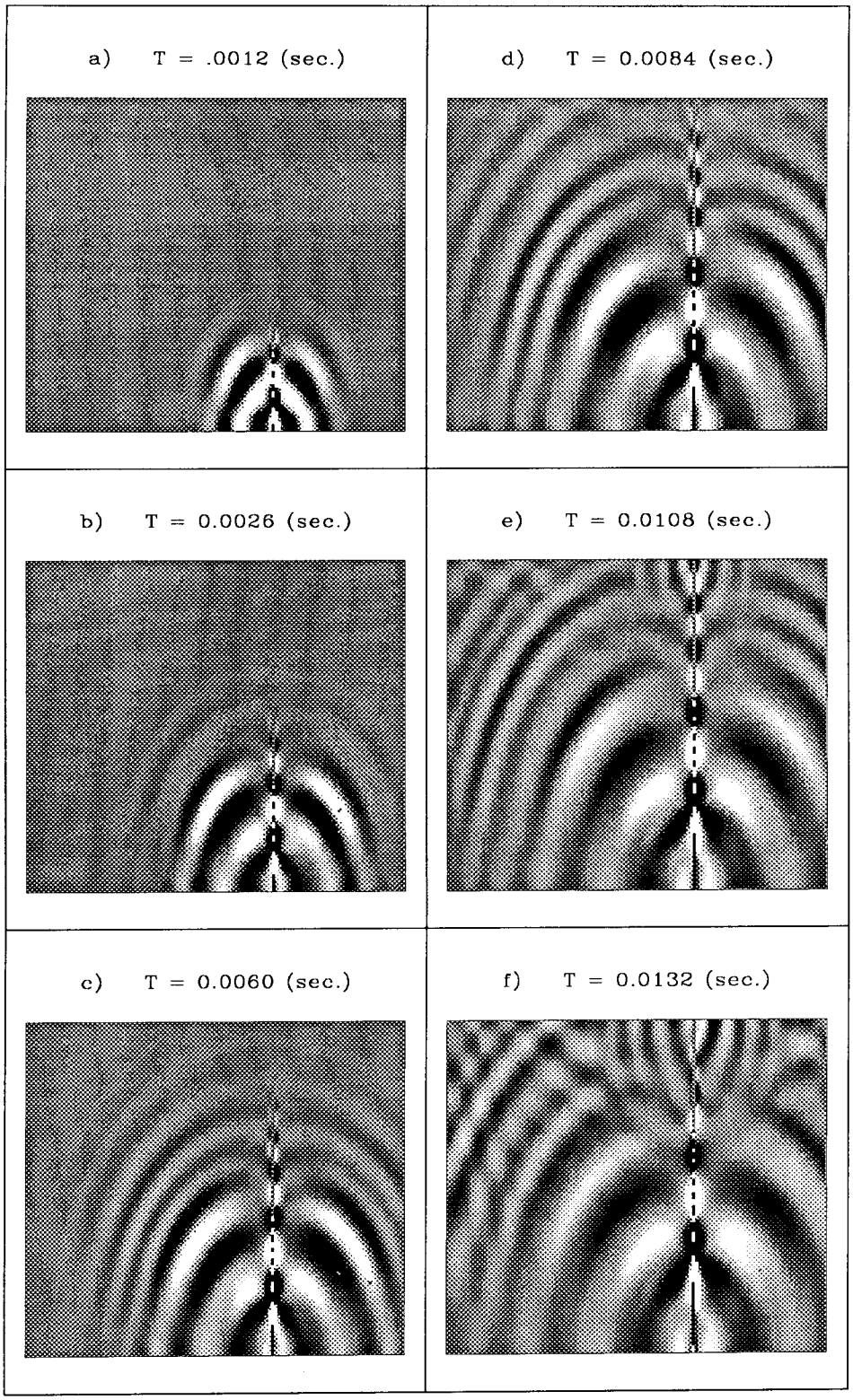

FIG. 6. Vertical displacements of the wavefield generated by a symmetrical pressure source at the bottom of the borehole. The medium surrounding the borehole is homogeneous.

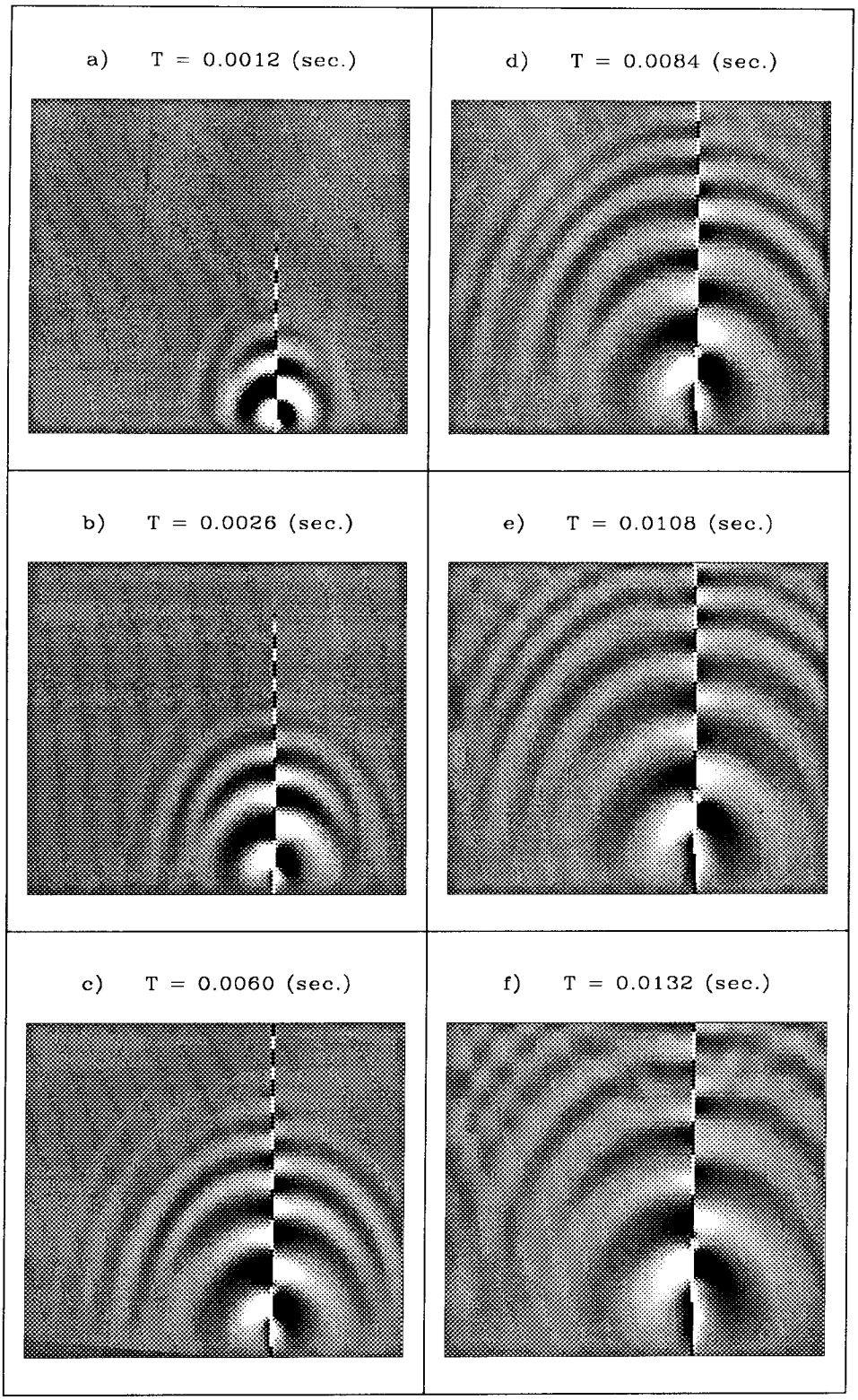

FIG. 7. Horizontal displacements of the wavefield generated by a symmetrical pressure source at the bottom of the borehole. The medium surrounding the borehole is homogeneous.

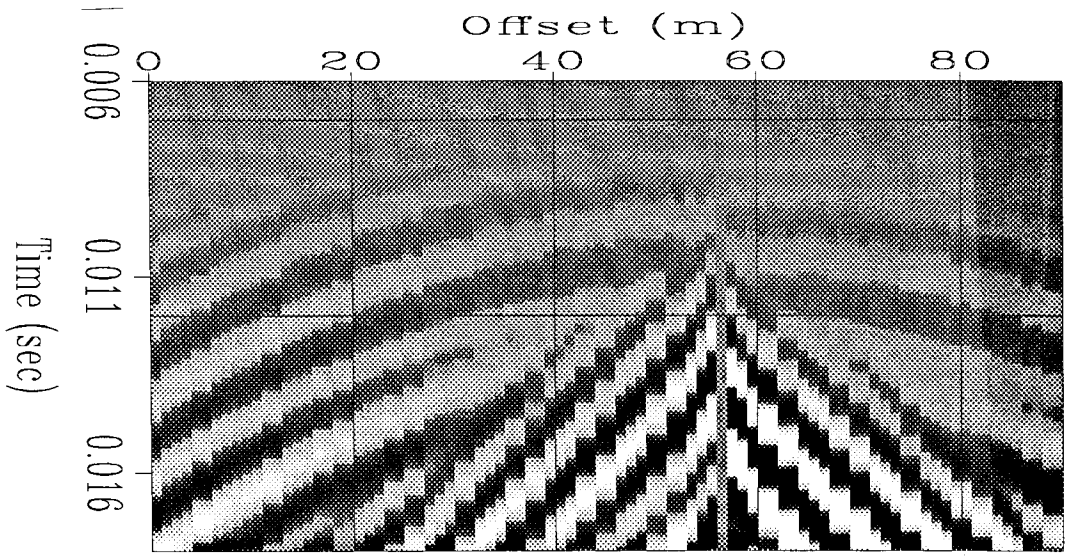

FIG. 8. Horizontal component of displacement recorded one meter below the free-surface. Same experiment as Figures 7.

Source in a fluid-filled borehole surrounded by a homogeneous medium: asymmetric source

The source is now composed of three point sources located on only the left side of the borehole. All other model parameters for this experiment are identical to those described in the previous example.

Several differences can be noted between experiments with symmetric and asymmetric sources. Figure 9.a shows the advance of phase for body waves on the same side of the borehole as the source.

Figure 7 showed a clear-cut opposition of phase for pseudo-Rayleigh waves on each side of the borehole, while Figures 9.b, 9.c, and 9.d suggest a time-variable phase difference between tube waves. If this indeed is the case, the time-variable phase difference could be explained as a superposition of two pseudo-Rayleigh modes – one symmetric (Figure 7), and one antisymmetric, or also flexural – propagating at a velocity slightly lower than the shear velocity (Barton et al., 1988).

The radiation pattern of the secondary source (Figures 9.f and 10.f) seems also asymmetric with stronger radiation to the side opposite the source. The asymmetry in the radiation pattern is related to the presence of an antisymmetric mode, and will therefore be dependent upon the length of the borehole.

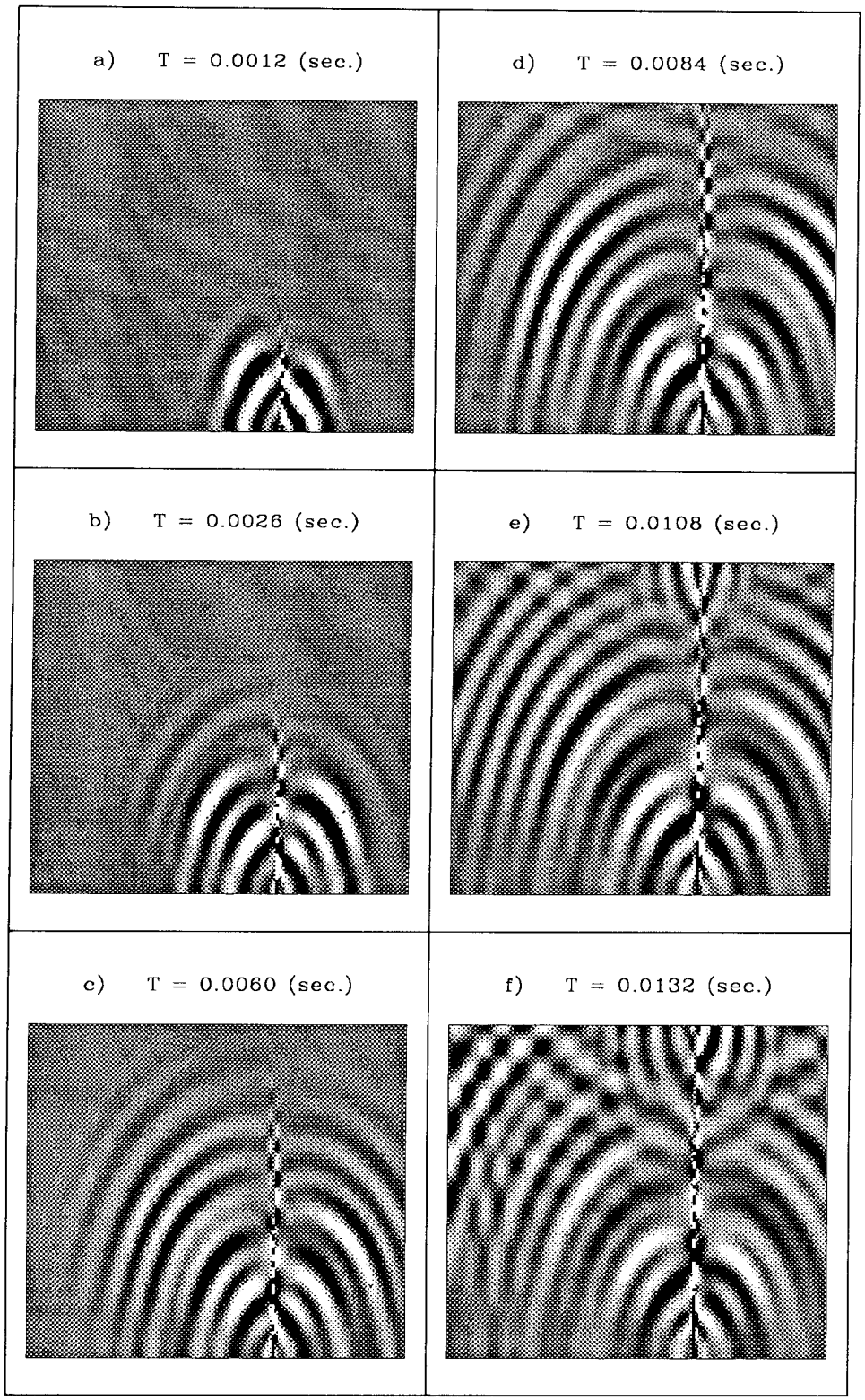

FIG. 9. Vertical displacements of the wavefield generated by a pressure source *asymmetrically* located at the bottom of the borehole. The medium surrounding the borehole is homogeneous.

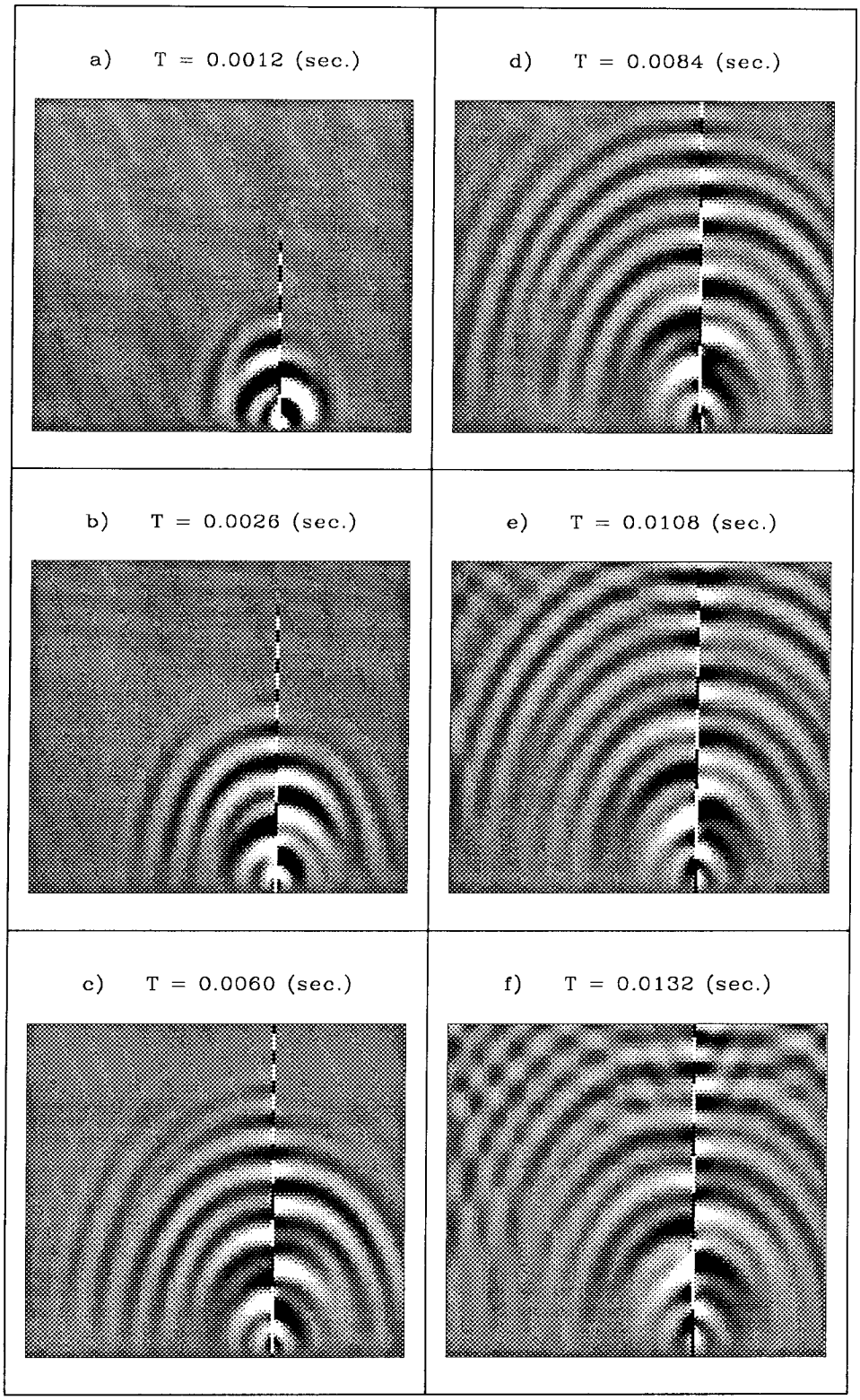

FIG. 10. Horizontal displacements of the wavefield generated by a pressure source *asymmetrically* located at the bottom of the borehole. The medium surrounding the borehole is homogeneous.

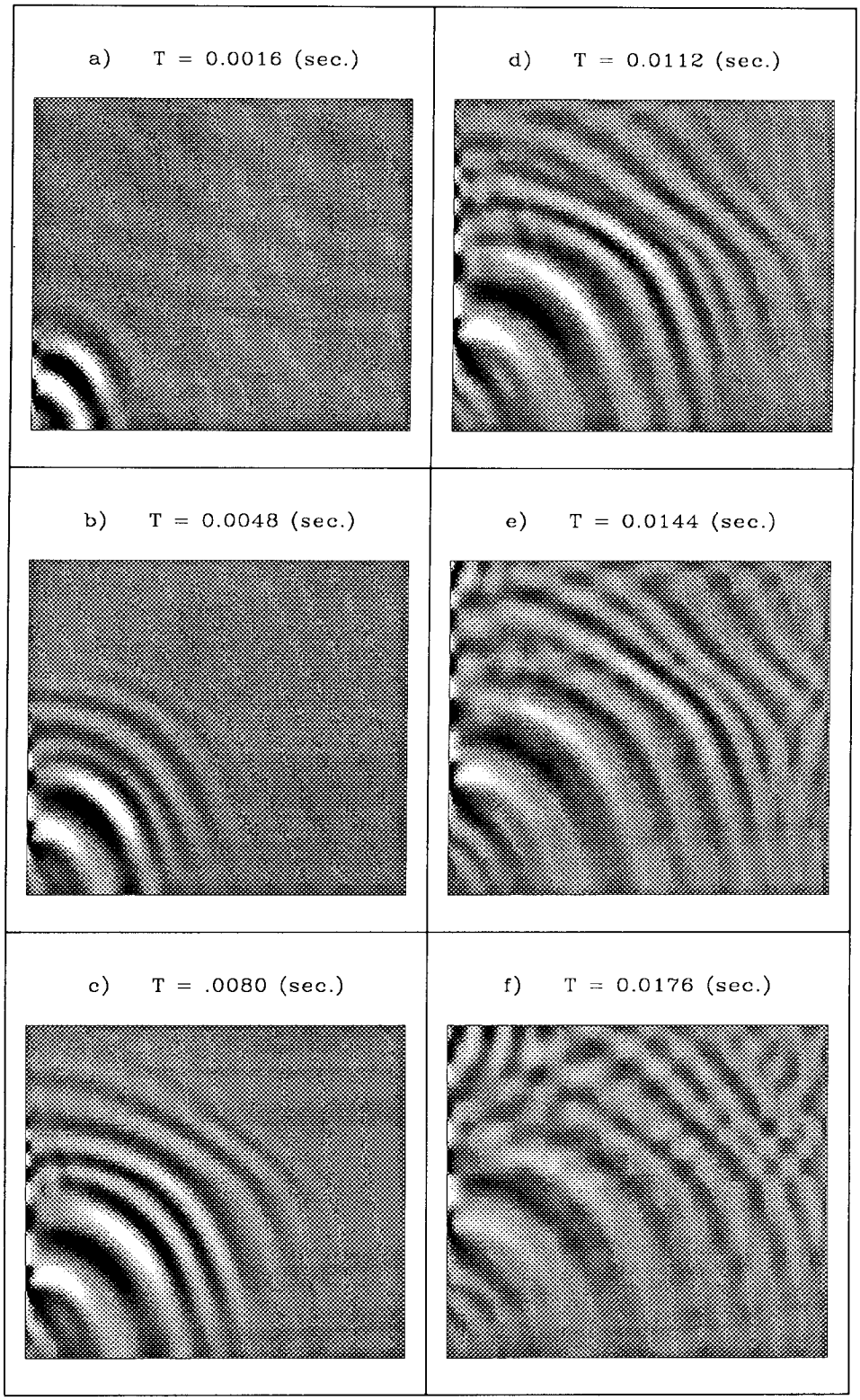

FIG. 11. Vertical displacements of the wavefield generated by a symmetric pressure source located at the bottom of the borehole. The medium surrounding the borehole is heterogeneous.

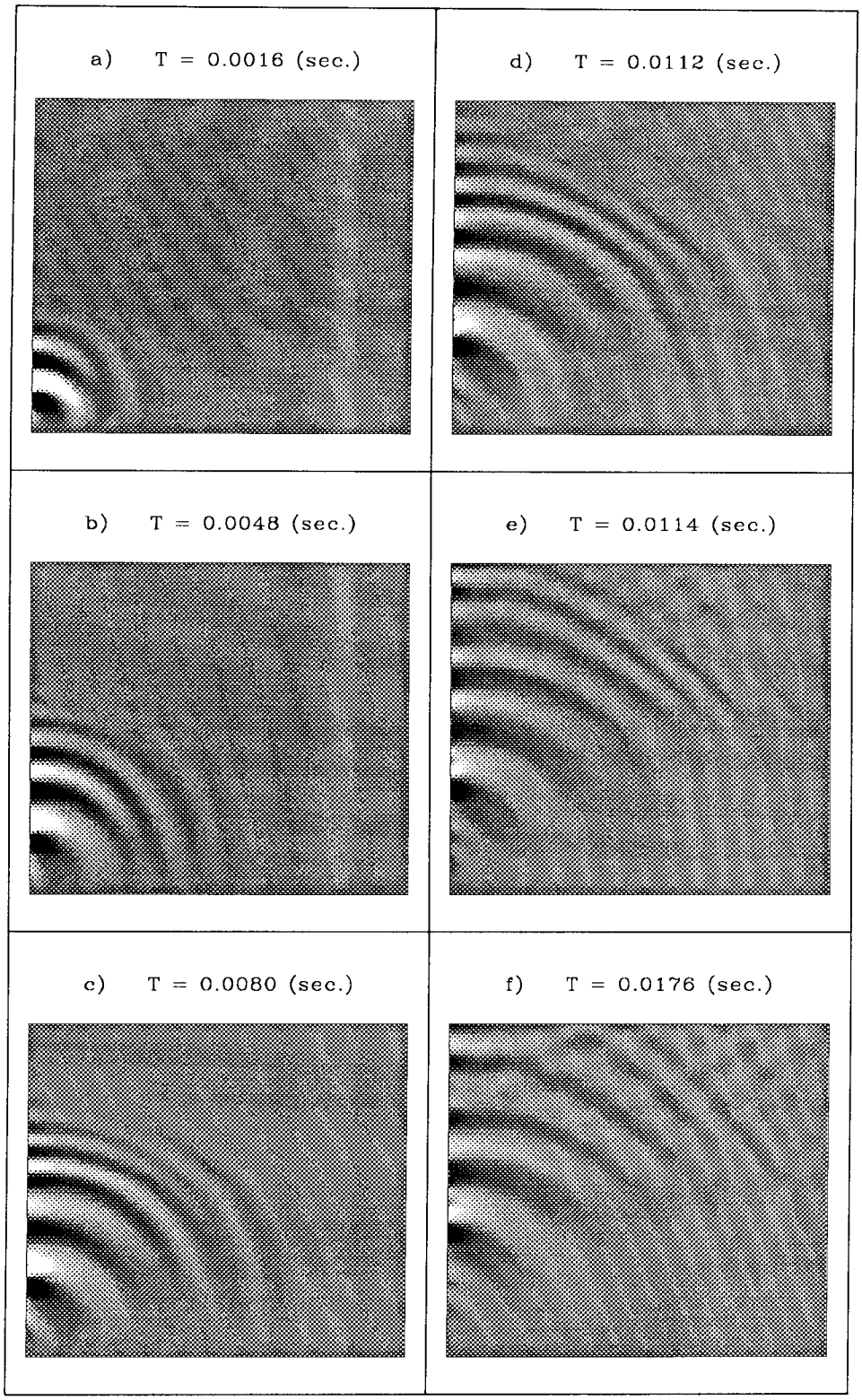

FIG. 12. Horizontal displacements of the wavefield generated by a symmetric pressure source located at the bottom of the borehole. The medium surrounding the borehole is heterogeneous.

Source in a fluid-filled borehole surrounded by a layered medium

The medium surrounding the borehole is composed of three layers, identical to those described in the section on modeling a point force in a heterogeneous medium (Figure 5).

At the layer boundaries tube waves are converted to body waves, as shown on Figures 11.c and 11.d for the vertical displacements, and on Figures 12.c and 12.d for the horizontal displacements of the wavefield. The implications are twofold (1) point sources along the borehole will radiate body waves, possibly leading to a model for a line source, (2) scattering along an irregular borehole surface will diminish the amplitude of the tube waves as well as the strength of the secondary point source at the head of the well (Figure 12.f). Depending on the relative strengths of these three types of sources – downhole source, scattering along the borehole surface, secondary source at the head of the well the processing of the data will be very different.

CONCLUSIONS

We obtained qualitative results about wave propagation at low frequencies in the neighborhood of a fluid-filled borehole. A most interesting observation is that tube waves can influence the far-field through conversions into body and surface waves at discontinuities along the borehole.

Directions for further work include the extension of the finite element code first to two space dimensions and cylindrical geometry, then to three space dimensions, so that amplitude variations of converted waves and focusing effects due to heterogeneities near the borehole could be more accurately accounted for. Observations of data from field experiments would help in selecting appropriate scales and parameters for models.

REFERENCES

Aki, K., and Richards, P. G., 1980, Quantitative seismology, theory and methods: W. H. Freeman and Co.

Barton C., Polarization of borehole tube waves, submitted to J. Geophys. Res.

Cheng. C.H., Toksoz, M.N., 1981, Elastic wave propagation in a fluid-filled borehole and synthetic acoustic logs: J. Geophys. Res., **87**, 5477-5848.

Claerbout, J., and Dellinger, J., 1986, Eisner's reciprocity paradox and its resolution: Leading Edge, **6**, 34-37.

Hughes T., 1984, The finite element method: Prentice Hall

Strang, G., 1986, Introduction to applied mathematics: Wellesley-Cambridge Press.

Sword C. 1986, Finite-element propagation of accoustic waves on a spherical shell: SEP-50.

Zienkiewicz, O., 1971, The finite element method in engineering science, McGraw-Hill